Research on Sea Surface Elliptical Current Remote Sensing With Single-Station Wide-Beam High-Frequency Sky–Surface Wave Radar

Mengyan Feng, Hanxian Fang, Xiongbin Wu, Weihua Ai, Xianchang Yue, and Lan Zhang

***Abstract*—This article describes a new elliptical current ($\vec{v}_{E-\text{ssw}}$) retrieval scheme for single-station wide-beam high-frequency sky–surface wave radar, which focuses on solving the problem of locating scattering patches on the sea surface. To start with, the measured data of the Digisonde portable sounder are exploited to correct the international reference ionosphere (IRI) model, which is capable of realizing the precise application of the IRI model to a certain extent. Subsequently, the scattering patches are located by combining the 3-D ray tracing and the corrected IRI model, and the radio wave incidence angles are obtained to calculate the theoretical Bragg frequency. Finally, the large-area elliptical currents are retrieved on the basis of the correction of sea echoes with ionosphere phase contamination extracted from direct waves. The effectiveness of this scheme is verified by comparing $\vec{v}_{E-\text{ssw}}$ with surface wave radar current products and by comparing with a location algorithm under the plane ionosphere assumption. The main achieved results are as follows. The predicted value of $\vec{v}_{E-\text{ssw}}$ by the location algorithm proposed in this article is more accurate than that obtained from the plane ionosphere location algorithm. The directions of $\vec{v}_{E-\text{ssw}}$ are in good agreement with the surface wave radar current product, and the root-mean-square error of $v_{E-\text{ssw}}$ is about 11.70 cm/s. In the detection core area, such an error is about 7.76 cm/s, and the scattering patches with smaller group paths exhibit higher retrieval accuracy of $v_{E-\text{ssw}}$. The relative error of $v_{E-\text{ssw}}$ in the core area demonstrates an ascending trend in the local time interval of 9:32–10:29, revealing that the effectiveness of this scheme could be affected by the ionosphere disturbance.**

***Index Terms*—International reference ionosphere (IRI) model correction, scattering patch location, sea surface current retrieval, wide-beam high-frequency hybrid sky–surface wave radar.**

I. Introduction

SEA surface current is a significant ocean dynamics parameter that plays a vital role in fishing, navigation, rescue, tsunami warning, and ocean environmental protection [1]. Since satellites and buoys are not able to perform large-area and continuous observation of specific sea regions [2], high-frequency radars have been widely used in coastal current monitoring [3]. Among the high-frequency radar systems, surface wave radar [4], [5], [6] and sky wave radar [7], [8] have particular limitations in remote sensing of large-area sea surface currents due to their short detection distance [4], [5] and severe ionosphere contamination [9].

Compared with surface wave radars and sky wave radars, sky–surface wave radars (HFSSWRs), with an inland sky wave transmitting station, are capable of continuously observing the target area by receiving surface waves at one station on the coastline or island [10], [11], [12], [13]. In this mode of operation, the corresponding ionosphere phase contamination is lower, and the flexible arrangement of receiving stations enables them to detect expansive ocean areas. Some scholars have conducted research on remote sensing of ocean dynamics parameters of HFSSWRs in recent decades, including theoretical modeling [14], [15], [16], [17], [18] and retrieval algorithm development [19], [20], [21]. Only sea surface current and wind direction have been reported for the remote sensing of sea states by HFSSWRs since the retrieval theory of these two parameters is more successful, and only the first-order scattering echoes are required. In the study of HFSSWR current retrieval, Ji et al. [19] retrieved the elliptical velocity with single-station wide-beam HFSSWR (SSWB-HFSSWR), and the root-mean-square error (RMSE) of 13.8 cm/s was derived by comparing the results with a current meter. However, the method of locating the sea surface scattering patches has not yet been introduced, so it was impossible to judge whether the elliptical velocity was located in the sea area where the current meter was located. Li et al. [21] established a combination algorithm of two receiving stations to locate the sea surface scattering patches and acquire the current vector. However, the proposed algorithm is implementable on the premise that both receiving stations must simultaneously receive the sea echoes, which is not always achievable, and the corresponding labor costs and computational efforts of the algorithm are high. Therefore, this article aims to use an SSWB-HFSSWR to carry out large-area elliptical current $\vec{v}_{E-\text{ssw}}$ retrieval (the component of the current vector, which is similar to the radial current of monostatic radar).

The location of scattering patches has always been an unresolved problem in sea state remote sensing with

Manuscript received 18 May 2023; revised 30 June 2023; accepted 20 August 2023. Date of publication 30 August 2023; date of current version 23 October 2023. This work was supported by the National Natural Science Foundation of China under Grant 61771352. *(Corresponding authors: Hanxian Fang; Xiongbin Wu.)*

Mengyan Feng, Hanxian Fang, and Weihua Ai are with the College of Meteorology and Oceanography, National University of Defense Technology, Changsha 410000, China (e-mail: fengmengyan18@nudt.edu.cn; fanghx@nudt.edu.cn; aiweihua19@nudt.edu.cn).

Xiongbin Wu, Xianchang Yue, and Lan Zhang are with the School of Electronic Information, Wuhan University, Wuhan 430072, China, and also with the Collaborative Innovation Center of Geospatial Technology, Wuhan 430079, China (e-mail: xbwu@whu.edu.cn; yuexc@whu.edu.cn; zhanglan@whu.edu.cn).

Digital Object Identifier 10.1109/JSTARS.2023.3310218

SSWB-HFSSWR. The main reason is that the instability of the ionosphere causes some difficulties in determining the sky-wave paths of radio waves (Sky_{path}). Generally, there exist two approaches to deriving Sky_{path} of radio waves [22]. The first is that the ionosphere is assumed as a plane, and the propagation paths of radio waves are modeled as straight lines [14], [16], [23], [24], which will lead to a significant error [25]. The second is to calculate Sky_{path} using 3-D ray tracing according to the electron density profile [26], [27]; however, the quality of the electron density profile affects the effectiveness of this method [28].

Owing to the high ionosphere variability and sparse arrangement of observation sites, the modeling of the real-time ionosphere is seldom examined, so the quasi-parabolic model is customarily employed in coordinate registration [29], [30]. This ionosphere model with a definite equation has few input parameters but its accuracy is limited. Compared with the quasi-parabolic model, the international reference ionosphere (IRI) model [31] successfully used in the middle latitudes is an empirical model based on a large amount of measured data from the ground, satellites, and rockets [32]. The most significant advantage of the IRI model is that it can provide electron density profiles at any time, latitude, and longitude. Many scholars utilize the measured data to evaluate the IRI model, refer to [33], [34], [35], [36], [37], [38], [39], [40], [41], [42], and [43]. The literature includes the comparison between the IRI model and the site-measured data, in which the sites are mainly located in the equatorial ionization anomaly edge region, and also the comparison with the International GNSS Service vertical total electron content maps. The data used to evaluate the IRI model cover the low and high solar activities, as well as quiet and turbulent geomagnetic conditions. The main conclusion is that the predicted results by the IRI model agree well with the measured data, particularly in the daytime with low solar activity and geomagnetic quiet conditions (e.g., $Kp < 3$). Although the IRI model performs well in describing the average behavior of the ionosphere, it still has limitations in precise application [42]. However, it is reported that the ionosphere has similar variations in thousands of kilometers horizontally and tens of kilometers vertically [44], [45], which supports us to use ionosphere measured data to correct the IRI model for precise application.

To realize the retrieval of large-area elliptical current $\vec{v}_{E-\text{ssw}}$ with SSWB-HFSSWR, a new retrieval scheme is proposed in this article. We first correct the IRI model with the measured data of the ionosphere observation site, which is capable of realizing the precise application of the IRI model to a certain extent. Then, the sea surface scattering patches are located by combining the multiple signal classification algorithm (MUSIC) and 3-D ray tracing. Finally, combined with the retrieval theory of $\vec{v}_{E-\text{ssw}}$, a large-area of $\vec{v}_{E-\text{ssw}}$ is obtained. Compared with the current products of surface wave radar, the effectiveness and feasibility of this scheme are verified. In addition, compared with the location algorithm under the plane ionosphere, this scheme has higher retrieval precision.

This article is organized as follows. Section II presents the dataset and the methodology utilized to conduct the research. Section III presents the results. The discussion is provided in Section IV. Finally, Section V concludes this article.

II. Data and Methods

A. Data

On April 4, 2017, the Radio Ocean Laboratory of Wuhan University simultaneously carried out remote sensing experiments of ocean dynamic parameters with two surface wave radars and SSWB-HFSSWR. The transmitting station of SSWB-HFSSWR is located at Wuhan University (30.54°N, 114.36°E), and the receiving station is located in Dongshan (23.65°N, 117.48°E), including two log-periodic antennas and eight-element monopole antennas. The sweep duration is 0.5 s, the coherent integration time is 5 min, the operation frequency of SSWB-HFSSWR is 10.66 MHz, and the range resolution is 10 km. E-layer echoes were received at 9:32, 9:44, 10:19, and 10:29 local times. The two surface wave radar stations are located in Dongshan and Chihu (24.0°N, 117.90°E), and the current vectors are retrieved every 10 min. Since the existing products of the surface wave radar have been demonstrated to be effective and accurate [21], [46], [47], [48], [49], they can be effectively adapted to verify the $\vec{v}_{E-\text{ssw}}$ accuracy of the SSWB-HFSSWR. Li et al. [21] verified the current retrieved by two WB-HFSSWRs with the current products of surface wave radar. Further details regarding these experiments and radars are available in [12].

During the experiment, the F10.7-index and *Kp*-index were reported to be 93.8 sfu and 2.66, respectively, which indicates low solar activity (F10.7<100 sfu) and geomagnetic quiet conditions. According to the analysis given in Section I, it can be inferred that the IRI model should be in reasonably good agreement with the ionosphere measurement during the experiment. The China Research Institute of Radio-wave Propagation constructed and operated a long-running ionospheric observation network covering mainland China. By taking the central region of the connection between the transmitting and the receiving station of the SSWB-HFSSWR as the main ionosphere reflection region (about 26.70°N, 116.04°E), the only observation site that could be exploited for the current investigation is the Zuolingzhen site (30.53°N, 114.61°E) in Wuhan, where deploys a Digisonde portable sounder (DPS) that measures the electron density profile every 15 min. In this article, we analyze the electron density profiles based on the IRI and DPS with time from 8:00 to 10:30 local time on April 4, 2017. Due to the availability of only one site, we could not analyze the spatial variability of the ionosphere in the main ionosphere reflection region. Therefore, the IRI electron density correction coefficients obtained from the Zuolingzhen site will be applied in the main ionosphere reflection region.

Fig. 1 shows the schematic diagram of remote sensing in the ocean environment by SSWB-HFSSWR (left-hand side) and the geographical distribution (right-hand side). On the left-hand side of Fig. 1, the direct waves (green lines) with a certain elevation angle are received by the receiving station after being reflected by the ionosphere, and the blue lines indicate Sky_{path} of the sea echoes. On the right-hand side of Fig. 1, the yellow dotted line

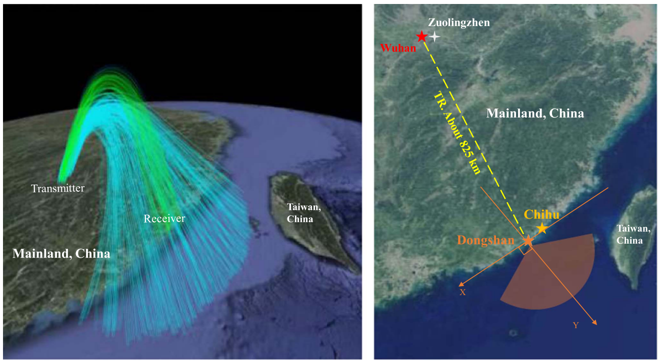

Fig. 1. Schematic representation of the remote sensing in the ocean environment by SSWB-HFSSWR (left-hand side) and the geographical distribution (right-hand side).

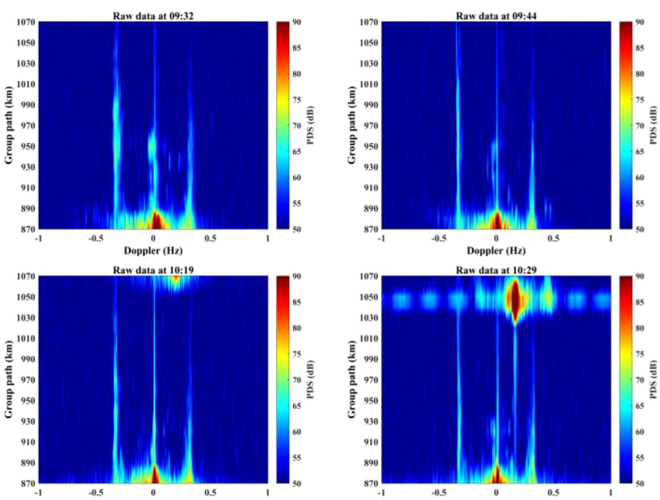

Fig. 2. Power density spectrum of range versus Doppler (RD spectrum).

TR connects the transmitting to the receiving station, where the corresponding interstation distance is about 825 km. The orange axis denotes the coordinate system with the receiving station as the origin while the *Y*-axis signifies the normal direction of the receiving antenna array, and the angle to the true north is 132°.

The power density spectrum of range versus Doppler (RD spectrum) has been depicted in Fig. 2. Signals with strong power near-zero Doppler represent direct waves, and it can be seen that the group path distance of the direct waves $\mathrm{GP}_{\mathrm{DW}}$ is about 870 km. There are positive and negative Bragg peaks on both sides of the direct wave. In the RD spectrum at 10:19 and 10:29, F-layer echoes with strong energy appeared at large group paths GP but F-layer echoes were not received at 9:32 and 9:44.

B. 3-D Ray Tracing Model

The 3-D ray tracing model, which mainly includes analytical [29], [50], [51], [52] and numerical [53], [54] models, is an effective technique to quantitatively calculate the propagation path of high-frequency radio waves in the ionosphere. The 3-D ray tracing model used in this article is shown in (1). The

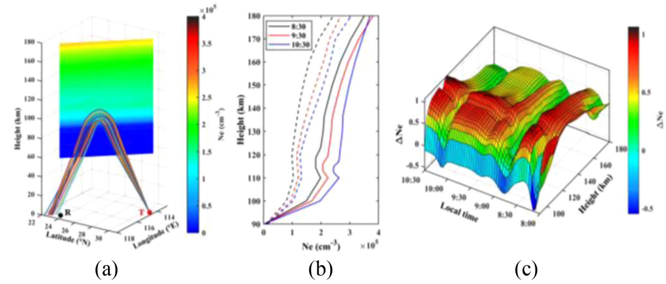

Fig. 3. (a) Propagation paths of radio waves with elevation angles of 10°–15° based on $Ne_{\mathrm{IRI}}(t,h)$. (b) $Ne_{\mathrm{DPS}}(t,h)$ and $Ne_{\mathrm{IRI}}(t,h)$ (dotted lines) at 8:30, 9:30, and 10:30 local time. (c) Curved surface of $\Delta Ne(t,h)$ distributed with local time and height.

Runge–Kutta methodology is implemented to solve the differential equations by combining them with the Appleton–Hartree equation [52], [53], [55]

$$\begin{cases} \frac{dr}{dP'} = \frac{c}{\omega} k_r \\ \frac{d\theta}{dP'} = \frac{c}{\omega r} k_\theta \\ \frac{d\varphi}{dP'} = \frac{c}{\omega r \sin\theta} k_\varphi \\ \frac{dk_r}{dP'} = -\frac{\omega}{2c}\frac{\partial X}{\partial \theta} + k_\theta^2 \frac{c}{\omega r} + k_\varphi^2 \frac{c}{\omega r} \\ \frac{dk_\theta}{dP'} = \frac{1}{r}\left(-\frac{\omega}{2c}\frac{\partial X}{\partial \theta} - k_r k_\theta \frac{c}{\omega} + k_\varphi^2 \frac{c}{\omega}\cot\theta\right) \\ \frac{dk_\varphi}{dP'} = \frac{1}{r\sin\theta}\left(-\frac{\omega}{2c}\frac{\partial X}{\partial \theta} - k_r k_\theta \frac{c}{\omega}\sin\theta + \frac{c}{\omega} k_\theta k_\varphi \cos\theta\right) \end{cases} \tag{1}$$

where P' denotes the group path, and r, θ, and φ represent the components of the location of the radio wave in spherical coordinates. The parameters k_r, k_θ, and k_φ are the magnitudes of the components of the radio wave number vector in the spherical coordinates. ω is the angular frequency, c is the speed of light, $X = f_N^2/f_0^2$, $f_N = 9.0\sqrt{Ne}$ is the plasma frequency, Ne is electron density, and f_0 is the radio wave frequency.

C. Correction of the IRI Model

Correcting the IRI model with measured data is a prerequisite for precise application. Taking the electron density calculated by the IRI model at 9:32 local time as an example, the propagation path of radio waves is simulated by 3-D ray tracing without any correction. We notice that no matter how the elevation angle is set, the radio waves cannot reach the receiving station, and the GP obtained by integrating propagation paths are also larger than $\mathrm{GP}_{\mathrm{DW}}$ (870 km), that is, the receiving station cannot receive any direct waves. The corresponding results are demonstrated in Fig. 3(a). In general, larger elevation angles have higher reflection heights and smaller ground distances. This pattern is met for the elevation angle of less than 13°, as shown in Fig. 3(a). However, in the case of the elevation angle greater than 13°, the radio wave is reflected more slowly and propagates a longer distance between the altitudes of 100 and 110 km, reaching a longer ground distance. As a result, we speculate that the IRI model underestimates the electron density between 100 and 110 km during the experiment.

We calculated the difference $\Delta Ne(t,h)$ between the measured data of the Zuolingzhen site and the electron density

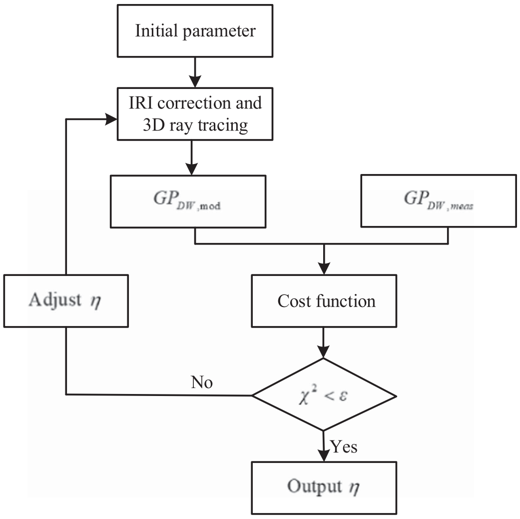

Fig. 4. Flowchart of the iterative process to determine η.

calculated by the IRI model in the range of 90–180 km

$$\Delta Ne(t,h) = \frac{Ne_{\text{DPS}}(t,h) - Ne_{\text{IRI}}(t,h)}{Ne_{\text{IRI}}(t,h)} \tag{2}$$

where $Ne_{\text{DPS}}(t,h)$ denotes the measured data and $Ne_{\text{IRI}}(t,h)$ represents the electron density calculated by the IRI model. t and h are local time and height, respectively.

Fig. 3(b) illustrates $Ne_{\text{DPS}}(t,h)$ and $Ne_{\text{IRI}}(t,h)$ (dotted lines) at 8:30, 9:30, and 10:30 local time. The depicted results indicate that $Ne_{\text{IRI}}(t,h)$ is smaller than $Ne_{\text{DPS}}(t,h)$, which is consistent with the speculation mentioned above. Fig. 3(c) shows the curved surface constructed by $\Delta Ne(t,h)$. It can be seen that the IRI model extremely underestimates the electron density within the range of 100–130 km, reaching the maximum more than one time. In addition, there is a valley between 110 and 120 km, which indicates that the IRI model has shortcomings in modeling the electron density in the valley layer compared with other heights.

Since there exists only one available ionosphere observation site for this experiment, it is fairly impossible to examine the variation of $\Delta Ne(t,h)$ with longitude and latitude. In this experiment, it is reasonable to use $\Delta Ne(t,h)$ for the sake of correcting the main reflection region, since the horizontal distance between the Zuolingzhen site and the main reflection region is about 448 km (less than 1000 km). In addition, a correction factor η is also added to fine-tune $\Delta Ne(t,h)$, and the IRI electron density in the main reflection region $Ne_{\text{IRI,MR}}(t,h)$ is corrected to

$$Ne_{\text{IRI,MR,Correct}}(t,h) = \eta \cdot (1 + \Delta Ne(t,h)) \cdot Ne_{\text{IRI,MR}}(t,h). \tag{3}$$

Prior information is also required to determine the value of η, and the relatively reliable prior information is GP_{DW}. Therefore, we construct a cost function χ^2 and determine η via the iterative method. The iterative process is schematically presented in Fig. 4.

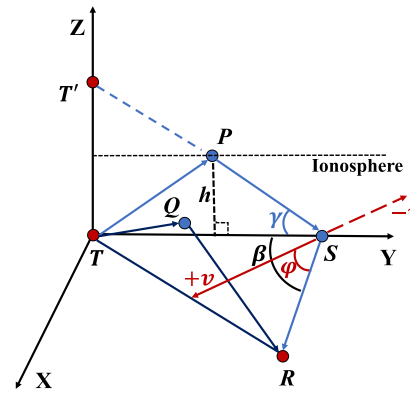

Fig. 5. Schematic diagram of the geometric relationship of $\vec{v}_{E-\text{ssw}}$ observed by the SSWB-HFSSWR.

The cost function χ^2 is defined as follows:

$$\chi^2 = \frac{[GP_{\text{DW,meas}} - GP_{\text{DW,mod}}]^2}{\sigma_{\text{GP}}^2} + \frac{[\eta - \eta_0]^2}{\sigma_{\eta_0}^2} \tag{4}$$

where $\text{GP}_{\text{DW,meas}}$ and $\text{GP}_{\text{DW,mod}}$ are measured and simulated GP_{DW}, respectively. σ_{GP} denotes the error of the measured GP_{DW} (since the range resolution of SSWB-HFSSWR is 10 km, σ_{GP} is set equal to 10 km), and η_0 is *a priori* estimate of η with *a priori* variance $\sigma_{\eta_0}^2$. The echoes of the E-layer are the most stable, and the horizontal distance between the Zuolingzhen site and the main reflection region is only a few hundred kilometers, so η does not substantially alter. Here, the values η_0 and σ_{η_0} are set as 1 and 0.5, respectively. What needs to be noted here is that different values of η_0 will not affect the results.

D. Elliptical Current Retrieval Method

SSWB-HFSSWR can be regarded as a special bistatic system. Fig. 5 presents a schematic diagram of the geometric relationship of $\vec{v}_{E-\text{ssw}}$ observed by the SSWB-HFSSWR. In this figure, the ionosphere is assumed to be a plane, and *P* and *Q* represent the ionosphere reflection points. In the algorithm for determining Sky_{path} under this assumption, *P* and *Q* have the same height h which can be calculated according to GP_{DW}. *T* is the transmitting station, *T′* is the symmetrical virtual image of *T*. *R* is the receiving station. *S* is the sea surface scattering patch. Furthermore, β denotes the bistatic angle, γ is the grazing incidence angle. The factors $+v$, $-v$ are $\vec{v}_{E-\text{ssw}}$ with opposite directions.

Since the transmitting station and receiving station of the SSWB-HFSSWR are not in a straight line, the direction of $\vec{v}_{E-\text{ssw}}$ is not on the line between the transmitting station and the sea surface scattering patch but depends on β and γ. The corresponding equation to this is as follows [21]:

$$\cos\varphi = \frac{\cos\beta\cos\gamma + 1}{\sqrt{1 + 2\cos\beta\cos\gamma + \cos^2\gamma}}. \tag{5}$$

The retrieval of $v_{E-\text{ssw}}$ requires a Doppler shift caused by the current f_c. After eliminating the Doppler shift caused by the ionosphere f_i (in this article, a generalized *S*-transform algorithm is used to eliminate f_i), f_c can be determined by the deviation of positive and negative first-order Bragg peaks (f_{b+}, f_{b-}) from their theoretical values $\pm f_B$ as follows:

$$\begin{cases} f_{b+} = f_B + f_c + f_i \\ f_{b-} = -f_B + f_c + f_i \\ f_B = \sqrt{(gf_0/2\pi c)(1+2\cos\beta\cos\gamma+\cos^2\gamma)^{1/2}} \end{cases} \quad (6)$$

where f_c and f_i represent the Doppler shifts caused by the current and ionosphere, respectively. The factor g denotes the gravitational acceleration and c denotes the speed of light. $v_{E-\text{ssw}}$ can be calculated by

$$v_{E-\text{ssw}} = \frac{f_c\lambda}{\sqrt{1+2\cos\beta\cos\gamma+\cos^2\gamma}}. \quad (7)$$

E. SSWB-HFSSWR Echo Data Preprocessing

Based on the 3-D ray tracing and the corrected IRI model, the illuminated sea area and Sky_{path} can be readily computed. The Sky_{path} plus the surface-wave path Sur_{path} between the receiving station and sea surface scattering patch is the group path of the sea echo GP_{sea}, that is, $\text{GP}_{\text{sea}} = \text{Sky}_{\text{path}} + \text{Sur}_{\text{path}}$. For the purpose of locating the sea surface scattering patches pertinent to the first-order scattering spectrum points, two basic steps are mandatory: 1) Extracting the first-order scattering spectrum points from the echo data. In order to make the extracted first-order spectrum points more accurate, we set the signal-to-noise ratio threshold to 10 dB and use the sliding window method to extract the first-order scattering spectrum points, as explained in [56]. The reason why we set the signal-to-noise ratio threshold to 10 dB is to avoid dividing the second-order spectrum points and noise into the first-order spectrum region. 2) Estimating the arrival directions of the first-order scattering spectrum points (DOA estimation). The MUSIC algorithm is employed for DOA estimation, see [57].

Correcting the ionosphere phase contamination is necessary before retrieving $\vec{v}_{E-\text{ssw}}$. In this article, the sea echoes are corrected by ionosphere phase contamination extracted from direct waves with a generalized *S*-transform algorithm, see [56], [58]. The overall flow is demonstrated in Fig. 6.

In this article, we also calculate Sky_{path} under the assumption of the plane ionosphere, and then, the sea surface scattering patches can be located. $\vec{v}_{E-\text{ssw}}$ corresponding to the plane ionosphere is also calculated and compared with $\vec{v}_{E-\text{ssw}}$ calculated by the retrieval scheme proposed in this article.

III. Results

Based on the corrected IRI model, Sky_{path} corresponding to the sea surface scattering patches can be calculated using a 3-D ray tracing, as demonstrated in Fig. 7(a). Only Sky_{path} corresponding to the 9:32 local time is shown here. It can be seen from Fig. 7(a) that Sky_{path} of the sea surface scattering patches increase with the ground distance. Fig. 7(b) shows γ associated with the sea surface scattering patches. The depicted results reveal that the variation of γ with the ground distance is opposite to that of Sky_{path}. It should be noted here that γ corresponding to the plane ionosphere is relatively large, about 17°–18°, which

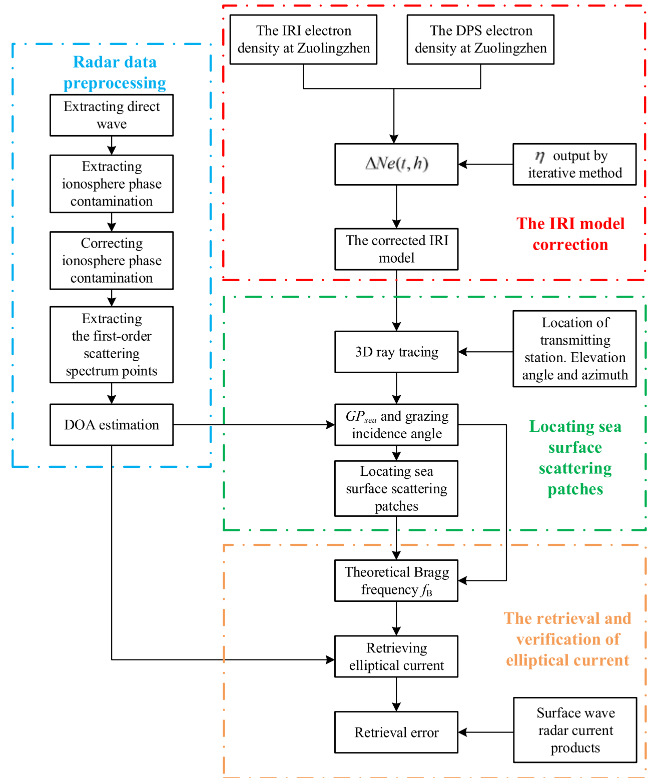

Fig. 6. Process diagram for retrieving $\vec{v}_{E-\text{ssw}}$ via the SSWB-HFSSWR.

will cause $\pm f_B$ corresponding to the two algorithms to be different.

The azimuth of the corrected first-order scattering spectrum points is determined by DOA estimation, and then, the corresponding value of Sur_{path} of spectrum points is determined by $\text{GP}_{\text{sea}} - \text{Sky}_{\text{path}}$; thereby, the locations of the sea surface scattering patches are determined on the map. The results of the locations are presented in Fig. 8. Different colored dots represent different values of GP_{sea}. Except for the echoes at 10:29 (there is a strong F-layer echo in the group distance larger than 1020 km), we locate the first-order scattering spectrum points in the range of 880–1070 km, since the signal-to-noise ratio in such an interval is larger, and the division of the first-order scattering spectrum region would be more precise. It can be seen that the farther the ground distance, the greater GP_{sea}. The sea surface scattering patches are uniformly distributed with the azimuth, basically showing a fan shape. These blue arrows represent the current vectors retrieved by using the surface wave radar, and the interpolation method is employed to complete the missing part. It should be also noticed here that since the surface wave radar did not work at 9:30, the current vectors presented in Fig. 8(a) were retrieved at 9:40. Because the sea surface current is stable for more than 10 min, it is reasonable to verify the $\vec{v}_{E-\text{ssw}}$ retrieved at 9:32 with the surface wave radar current vectors at 9:40.

The difference between the location results of the two algorithms is not easy to distinguish in the figure, and the sea surface scattering patches associated with the plane ionosphere are not shown in Fig. 8. We calculated that the average distance

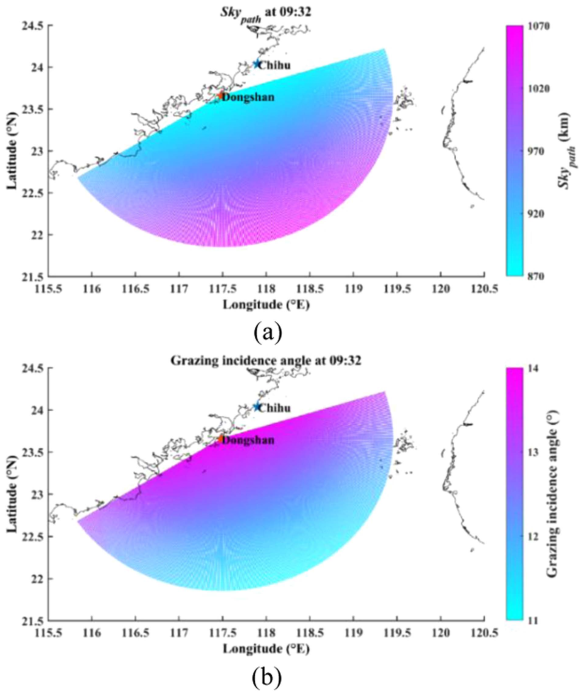

Fig. 7. Sky_{path} and γ associated with the sea surface scattering patches at 09:32 local time. (a) Sky_{path}. (b) γ.

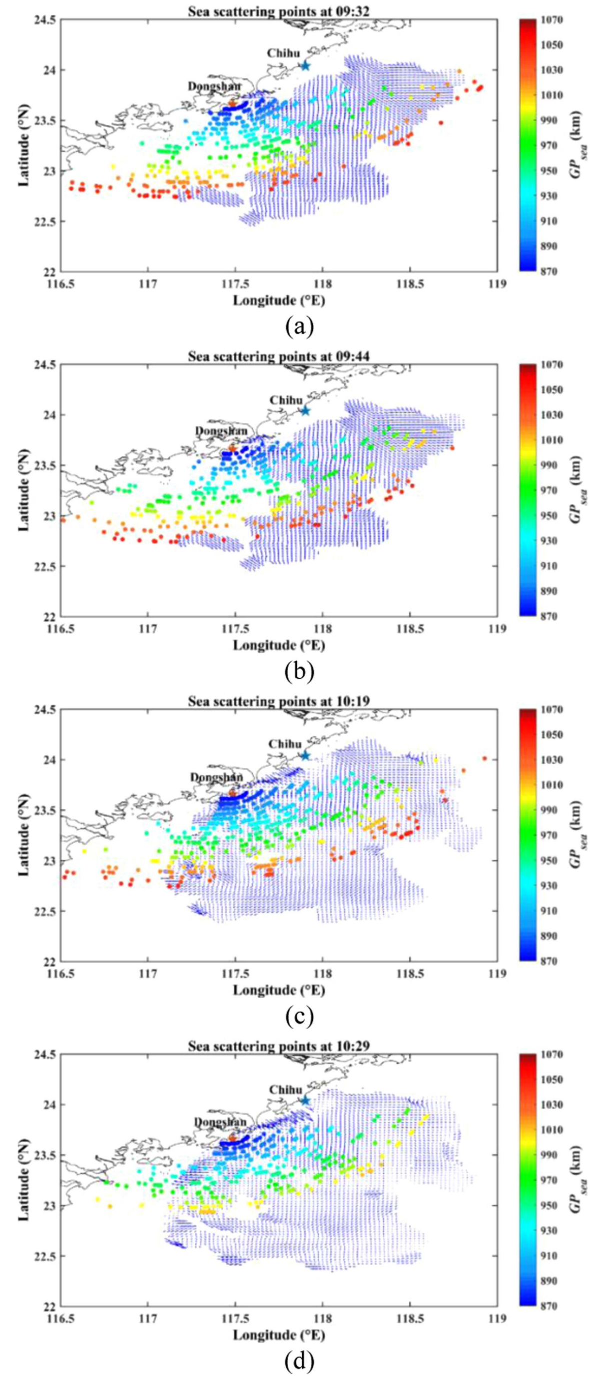

Fig. 8. Location of the sea surface scattering patches. (a) 09:32. (b) 09:44. (c) 10:19. (d) 10:29.

between scattering patches corresponding to the two algorithms is 0.48 km.

Each sea surface scattering patch corresponds to a radio wave propagation path calculated by 3-D ray tracing. The theoretical Bragg frequency $\pm f_B$ is calculated based on the incidence attitude of the radio wave, namely, the locations of the scattering patch and receiving station. In this article, the generalized *S*-transform is employed to correct the ionosphere phase contamination before retrieving $\vec{v}_{E-\mathrm{ssw}}$; therefore, the discrepancies between the Doppler of first-order scattering spectrum points and $\pm f_B$ are considered to be caused only by $\vec{v}_{E-\mathrm{ssw}}$. Based on the calculation method explained in Section II-D, the value $\vec{v}_{E-\mathrm{ssw}}$ is retrieved at each scattering patch. The results are shown in Fig. 9, and the red arrows indicate $\vec{v}_{E-\mathrm{ssw}}$. Simultaneously, the projection $\vec{v}_{E-\mathrm{sw}}$ of surface wave radar current vectors in the directions of $\vec{v}_{E-\mathrm{ssw}}$ is also displayed in Fig. 9, which are represented by blue arrows. It can be seen that, except for a few scattering patches adjacent to the edge region, the directions of $\vec{v}_{E-\mathrm{ssw}}$ and $\vec{v}_{E-\mathrm{sw}}$ of other scattering patches are almost identical, revealing that the directions of $\vec{v}_{E-\mathrm{ssw}}$ are basically correct.

To verify the accuracy of $v_{E-\mathrm{ssw}}$, the RMSE is calculated, and the relevant statistical results are presented in Table I (the value to the left of "/"). In addition, a core region (e.g., 117.5–118.2°E, 23–23.6°N) is defined, and the RMSE of $v_{E-\mathrm{ssw}}$ is calculated in this region. As seen from Table I, the RMSE of the core region is smaller than that of the whole area, which could be attributed to the following two reasons. 1) In the process of current vector synthesis with the two surface wave radars, there exists a large angle between the radial current in the middle

TABLE I
STATISTICAL ANALYSIS OF RETRIEVAL RESULTS OF $v_{E-\mathrm{ssw}}$

	Whole area		Core region		
time	N	RMSE (cm/s)	N	RMSE (cm/s)	RE (%)
9:32	416	13.39 / 13.21	147	5.15 / 5.08	17.0 / 16.5
9:44	358	10.75 / 11.60	119	8.13 / 8.83	27.7 / 28.8
10:19	448	10.77 / 11.17	157	9.24 / 10.07	55.5 / 59.7
10:29	328	11.61 / 15.02	133	7.86 / 10.73	49.1 / 88.5
All	1550	11.70 / 12.71	556	7.76 / 8.17	37.8 / 44.6

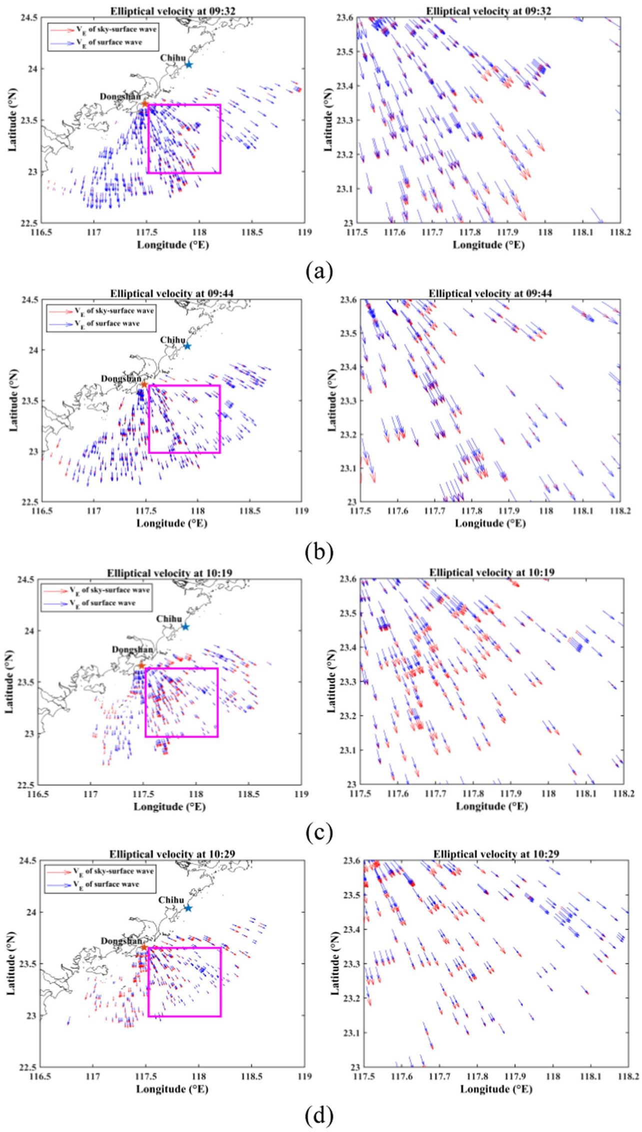

Fig. 9. Retrieval results of $\vec{v}_{E-\mathrm{ssw}}$ (the left-hand side is the whole area, and the right-hand side is the core region). (a) 09:32. (b) 09:44. (c) 10:19. (d) 10:29.

sea area close to the two radar stations; hence, it often has high synthesis accuracy in the core region. 2) The ionosphere reflection region associated with the core region is closer to the ionosphere reflection region of the direct wave; as a result, the ionosphere phase contamination extracted from the direct wave is more effective in the core region.

Table I also shows the relative error (RE) of $v_{E-\mathrm{ssw}}$ within the core area (the value to the left of "/"). It can be seen that the REs at 9:32 and 9:44 are relatively small, with 17.0% and 27.7%, respectively. REs at 10:19 and 10:29 are larger, with 55.5% and 49.1%, respectively. We speculate that the reason for this phenomenon is that the ionosphere becomes unstable as a result of the impact of solar radiation as the time approaches the local noon. The instability of the ionosphere will cause the propagation paths of radio waves to considerably alter, resulting in a long distance between the sea areas illuminated by the radio wave with the same elevation and azimuth angles in a coherent integration time. Even the corrected IRI model is only capable of representing a highly accurate average behavior of the ionosphere within a coherent integration time and could not properly respond to the rapid variation of electron density. It can also be seen from Fig. 1 that there are no F-layer echoes in the RD spectrum at 9:32 and 9:44, the direct wave reflected by the F-layer initiates to appear at about 1070 km in the RD spectrum at 10:19, and the direct wave reflected by the F-layer, with GP_{DW} reduced to about 1030 km, completely appears in the RD spectrum at 10:29. These phenomena indicate that the electron density in the F-layer progressively magnifies during this time owing to the influence of the solar radiation, which also affects the lower E-layer.

TABLE II
$v_{E-\mathrm{ssw}}$ RETRIEVAL ACCURACY OF DIFFERENT INTERVALS IN THE CORE REGION

	Interval 1		Interval 2		Interval 3	
time	N	RMSE (cm/s)	N	RMSE (cm/s)	N	RMSE (cm/s)
9:32	46	2.49	78	5.44	23	7.58
9:44	38	4.39	49	6.94	32	12.33
10:19	55	6.94	55	9.82	47	10.76
10:29	28	6.16	52	8.01	53	8.48

We also calculate the RMSE and RE of $v_{E-\mathrm{ssw}}$ corresponding to the plane ionosphere, and the results have been presented in Table I (the value to the right of "/"). It can be seen that the RMSE and RE corresponding to the plane ionosphere at 9:32 are lower than the algorithm proposed in this article, and the performance of the plane-ionosphere-based location algorithm is not as good as the algorithm proposed in this article for the data at other times. The reason for this is that the surface wave radar current product employed to verify $v_{E-\mathrm{ssw}}$ at 9:32 is at 9:40, which will affect the comparison of the two location algorithms. In the whole region, the $v_{E-\mathrm{ssw}}$ retrieval accuracy corresponding to the location algorithm proposed in this article is improved by 7.9% compared with $v_{E-\mathrm{ssw}}$ corresponding to the plane ionosphere location algorithm, and its improvement in the core region is 5%.

The three intervals in the core region are suitably divided according to GP_{sea}, which are 880–930 km, 940–990 km, and 1000–1070 km, respectively, and subsequently, the RMSE is calculated for each interval. The results are shown in Table II. It can be seen that the larger GP_{sea} of sea echo, the greater RMSE of $v_{E-\mathrm{ssw}}$. What requires to be elucidated here is that since the echoes of the F-layer occupy about five range bins in the 10:29 RD spectrum, the three intervals are 880–920 km, 930–970 km, and 980–1020 km, respectively, the so-called interval 1, interval 2, and interval 3.

IV. DISCUSSION

The research of this article involves various aspects. The algorithms involved in radar data preprocessing in Fig. 6, such as the extraction of direct wave and first-order scattering spectrum points, ionosphere phase contamination correction, and MUSIC, could be readily found in the literature; therefore, these signal processing algorithms are not introduced again in detail.

In this experiment, the horizontal distance between the Zuolingzhen site and the main reflection region of the ionosphere is about 448 km; hence, it is considered that the ionosphere in the two places has the same variation. In addition, the solar activity is low and the geomagnetic field is quiet during the experiment, indicating that the IRI model has a good influence on the ionospheric prediction. As a result, it is possible to utilize the DPS data of the Zuolingzhen site to correct the IRI electron density in the main reflection region. For the purpose of achieving the best correction effect, a correction factor η is introduced and the optimal value of η could be appropriately calculated by the iterative method, which gives more precise electron density data for the 3-D ray tracing to locate sea surface scattering patches. Based on the retrieval accuracy of $v_{E-\mathrm{ssw}}$ at 9:32 and 9:44, the calculation results indicate that the sea surface scattering patch location method based on the 3-D ray tracing and the corrected IRI model performs better when the ionosphere is stable. The decrease in the retrieval accuracy of $v_{E-\mathrm{ssw}}$ at 10:19 and 10:29 indicates that the ionospheric instability could affect the accuracy of the location method. It is also worth mentioning here that the statistical results given in Table I show that the RMSE of $v_{E-\mathrm{ssw}}$ at 10:29 is less than that of 9:44 and 10:19, which is chiefly attributed to the sea echoes of the larger range bins being missing at 10:29 due to the contamination of F-layer. We believe that increasing the temporal resolution of electron density data could enhance the location accuracy of scattering patches in the presence of serious ionosphere disturbances, since such a severe circumference allows the application of 3-D ray tracing in finer temporal intervals. Therefore, it is very important to construct ionosphere observation sites in the main ionosphere reflection region. For the cases of high solar activity and turbulent geomagnetic conditions, relevant experiments should be performed to assess the effectiveness of this new $\vec{v}_{E-\mathrm{ssw}}$ retrieval scheme.

The location algorithm based on 3-D ray tracing could obtain the value of $v_{E-\mathrm{ssw}}$ with higher accuracy. There are two reasons for the difference in the retrieval results of the two location algorithms. 1) The location of sea surface scattering patches is different, with an average difference of 0.48 km, which has great influence when the spatial variability of current vectors is large. 2) The incidence angles of radio waves on the sea surface are different, with a difference of about 4°, which will lead to differences in the calculation of theoretical Bragg frequency, thus affecting the retrieval accuracy of $v_{E-\mathrm{ssw}}$.

In addition to the location accuracy of scattering patches, ionosphere phase contamination also expresses an influential factor that seriously influences the retrieval accuracy of $v_{E-\mathrm{ssw}}$. It is reasonable to use the ionosphere phase contamination extracted from direct waves to correct sea echoes, but it is inevitable that sea echoes with reflection regions closer to those of direct waves have a better correction effect. Such a fact is also confirmed by the results provided in Table II, that is, sea echoes with smaller $\mathrm{GP}_{\mathrm{sea}}$ exhibit higher retrieval accuracy. Therefore, how to correct the ionosphere phase contamination accurately for sea echoes with large $\mathrm{GP}_{\mathrm{sea}}$ is a problematic issue that should be unlocked in the near future. In general, two solutions could be followed. 1) A number of ionosphere observation sites should be constructed in the main ionosphere reflection region to obtain high temporal resolution electron density data at several locations and to construct a real-time ionosphere model for this region. 2) Reference sources, such as islands or transponders, should be set up in distant sea areas, and the ionosphere phase contamination is extracted from the signals reflected by the islands and the signals received by the transponders to modify the sea echoes. It is worth noting that the ionosphere phase decontamination algorithm is not the only issue affecting the results presented in Table II but also the spatial variability of current vectors is another critical item. Because the sea area illuminated by radio waves will change dynamically under the ionosphere disturbance conditions, large spatial variability of currents (such as eddy) could lead to a large difference of current information carried in scattered signals, hence yielding retrieval errors.

The innovation of this article is that we introduce the measured ionosphere data so that the IRI model can be applied to the location of sea surface scattering patches, which provides a more effective method than the plane ionosphere. This article is also an attempt at the IRI model in fine application, which expands the application field of the IRI model to some extent. This work lays a technical foundation for solving the current vector retrieval of SSWB-HFSSWR in the future.

V. Conclusion

To retrieve the large-area $\vec{v}_{E-\mathrm{ssw}}$ from sea echoes of an SSWB-HFSSWR, we present an IRI model correction algorithm based on the measured data of the ionosphere by realizing the location of sea surface scattering patches by combining the 3-D ray tracing. On the basis of correcting the ionosphere phase contamination of sea echoes, the large-area $\vec{v}_{E-\mathrm{ssw}}$ is retrieved. The main conclusions are as follows.

1) In the experiment, the IRI model underestimates the electron density of the E-layer, and the modeling of the electron density in the valley layer is inconsistent.
2) Except for a few scattering patches close to the edge region, the directions of $\vec{v}_{E-\mathrm{ssw}}$ are basically correct.
3) The location algorithm based on 3-D ray tracing has higher retrieval accuracy of $v_{E-\mathrm{ssw}}$, which shows that the algorithm is more effective than the location algorithm based on the plane ionosphere.
4) $v_{E-\mathrm{ssw}}$ in the core area has higher retrieval accuracy than that in the whole region, with RMSE values of 7.76 cm/s and 11.70 cm/s, respectively. The key reasons are that the quality of $\vec{v}_{E-\mathrm{sw}}$ in the core area is high, and the ionosphere phase decontamination algorithm performs better in the core area.
5) In the core area, $v_{E-\mathrm{ssw}}$ with smaller $\mathrm{GP}_{\mathrm{sea}}$ has higher retrieval accuracy, since the reflection region of the sea echo with smaller $\mathrm{GP}_{\mathrm{sea}}$ is closer to that of the direct wave, and ionosphere phase contamination extracted from the direct wave exhibits a better correction effect for these sea echoes.

6) During the time interval 9:32–10:29, the retrieval accuracy of $v_{E-\mathrm{ssw}}$ in the core area demonstrates a descending trend. The main reason behind this fact is that by growing the solar radiation (F-layer echo gradually appears in the RD spectrum), the instability of the ionosphere would influence the location accuracy of the scattering patches.

Since there is no ADCP current data in this sea area, we use the current products of surface wave radar to verify the algorithm, which is a defect of this article. In the future, we will use ADCP current data to verify our proposed algorithm in other sea areas.

Author Contributions

Mengyan Feng conducted all programming, calculations, and comparisons; he was also responsible for the figures and general text. Hanxian Fang, Weihua Ai, and Xiongbin Wu took part in the literature review and analysis. Xianchang Yue and Lan Zhang took part in all discussions and analyses at all stages of the research. All authors have read and agreed to the published version of the article.

Declaration of Interest Statement

The authors declare that they have no known competing financial interests or personal relationships that could have appeared to influence the work reported in this article.

Acknowledgment

The authors acknowledge the use of data from the Chinese Meridian Project.

References

[1] D. E. Barrick, "A coastal radar system for tsunami warning," *Remote Sens. Environ.*, vol. 8, no. 4, pp. 353–358, 1979.

[2] M. Feng, W. Ai, W. Lu, C. Shan, S. Ma, and G. Chen, "Sea surface temperature retrieval based on simulated microwave polarimetric measurements of a one-dimensional synthetic aperture microwave radiometer," *Acta Oceanologica Sinica*, vol. 40, no. 3, pp. 122–133, 2021.

[3] D. E. Barrick, M. W. Evans, and B. L. Weber, "Ocean surface currents mapped by radar," *Science*, vol. 198, no. 4313, pp. 138–144, 1977.

[4] W. Huang, S. Wu, E. Gill, B. Wen, and J. Hou, "HF radar wave and wind measurement over the Eastern China Sea," *IEEE Trans. Geosci. Remote Sens.*, vol. 40, no. 9, pp. 1950–1955, Sep. 2002.

[5] K. W. Gurgel, G. Antonischki, H. H. Essen, and T. Schlick, "Wellen Radar (WERA): A new ground-wave HF radar for ocean remote sensing," *Coastal Eng.*, vol. 37, no. 3, pp. 219–234, 1999.

[6] M. W. Evans and T. M. Georges, "Coastal ocean dynamics radar (CODAR): NOAA's surface current mapping system," in *Proc. Oceans*, 1979, pp. 379–384.

[7] J. R. Barnum, "Skywave polarization rotation in swept-frequency sea backscatter," *Radio Sci.*, vol. 8, no. 5, pp. 411–423, 1973, doi: 10.1029/RS008i005p00411.

[8] J. Barnum, J. Maresca, and S. Serebreny, "High-resolution mapping of oceanic wind fields with skywave radar," *IEEE Trans. Antennas Propag.*, vol. TAP-25, no. 1, pp. 128–132, Jan. 1977.

[9] T. Georges, "Progress toward a practical skywave sea-state radar," *IEEE Trans. Antennas Propag.*, vol. TAP-28, no. 6, pp. 751–761, Nov. 1980.

[10] R. J. Riddolls, "Ship detection performance of a high frequency hybrid sky-surface wave radar," Defense R&D Canada-Ottawa, 2007.

[11] Z. Zhao, X. Wan, D. Zhang, and F. Cheng, "An experimental study of HF passive bistatic radar via hybrid sky-surface wave mode," *IEEE Trans. Antennas Propag.*, vol. 61, no. 1, pp. 415–424, Jan. 2013.

[12] Z. Lan, W. Xiongbin, L. Jianfei, L. Zhengyong, and C. Xiaofeng, "A study on hybrid networking system for distributed HF over-the-horizon radars," in *Proc. XXXIth URSI Gen. Assem. Sci. Symp.*, 2014, pp. 1–4.

[13] I. S. Turgenev and P. A. Melyanovcky, "Bistatic HF radar for oceanography applications with the use of both ground and space waves," *Telecommun. Radio Eng.*, vol. 51, no. 2/3, pp. 73–80, 1997.

[14] J. Walsh, E. W. Gill, W. Huang, and S. Chen, "On the development of a high-frequency radar cross section model for mixed path ionosphere–ocean propagation," *IEEE Trans. Antennas Propag.*, vol. 63, no. 6, pp. 2655–2664, Jun. 2015.

[15] L. Ya-jun, W. Yin-sheng, Z. Yong-peng, G. Ru-jiang, W. Zhuo-qun, and X. Rong-qing, "Analysis and simulation for broadening first-order sea clutter spectrum in high frequency hybrid sky-surface wave propagation mode," *IET Radar, Sonar, Navigation*, vol. 9, no. 6, pp. 609–621, 2015, doi: 10.1049/iet-rsn.2014.0008.

[16] S. Chen, E. W. Gill, and W. Huang, "A first-order HF radar cross-section model for mixed-path ionosphere–ocean propagation with an FMCW source," *IEEE J. Ocean. Eng.*, vol. 41, no. 4, pp. 982–992, Oct. 2016.

[17] S. Chen, E. W. Gill, and W. Huang, "A second-order monostatic high frequency radar power model for mixed-path propagation," in *Proc. 17th Int. Symp. Antenna Technol. Appl. Electromagn.*, 2016, pp. 1–2.

[18] S. Chen, E. W. Gill, and W. Huang, "A high-frequency surface wave radar ionospheric clutter model for mixed-path propagation with the second-order sea scattering," *IEEE Trans. Antennas Propag.*, vol. 64, no. 12, pp. 5373–5381, Dec. 2016.

[19] Y. Ji, J. Zhang, X. Chu, Y. Wang, and L. Yang, "Ocean surface current measurement with high-frequency hybrid sky–surface wave radar," *Remote Sens. Lett.*, vol. 8, no. 7, pp. 617–626, 2017.

[20] X. Chu, J. Zhang, Y. Ji, Y. Wang, and L. Yang, "Extraction of wind direction from the HF hybrid sky-surface wave radar sea echoes," *IEEE Aerosp. Electron. Syst. Mag.*, vol. 33, no. 3, pp. 42–47, Mar. 2018.

[21] M. Li et al., "Ocean surface current extraction scheme with high-frequency distributed hybrid sky-surface wave radar system," *IEEE Trans. Geosci. Remote Sens.*, vol. 56, no. 8, pp. 4678–4690, Aug. 2018.

[22] Z. Guo, Z. Wang, Y. Hao, H. Lan, and Q. Pan, "An improved coordinate registration for over-the-horizon radar using reference sources," *Electronics*, vol. 10, no. 24, 2021, Art. no. 3086.

[23] G. W. Pulford and R. J. Evans, "A multipath data association tracker for over-the-horizon radar," *IEEE Trans. Aerosp. Electron. Syst.*, vol. 34, no. 4, pp. 1165–1183, Oct. 1998.

[24] Z. Guo, Z. Wang, H. Lan, Q. Pan, and K. Lu, "OTHR multitarget tracking with a GMRF model of ionospheric parameters," *Signal Process.*, vol. 182, 2021, Art. no. 107940.

[25] C. J. X. Zhang, T. Liu, G. Yang, and Z. Zhao, "Effect of the ionospheric virtual height on the joint positioning accuracy of multi-station over-the-horizon radar system," *Chin. J. Radio Sci.*, vol. 37, no. 5, pp. 761–767, 2022.

[26] R. H. Anderson and J. L. Krolik, "Track association for over-the-horizon radar with a statistical ionospheric model," *IEEE Trans. Signal Process.*, vol. 50, no. 11, pp. 2632–2643, Nov. 2002.

[27] K. Romeo, Y. Bar-Shalom, and P. Willett, "Detecting low SNR tracks with OTHR using a refraction model," *IEEE Trans. Aerosp. Electron. Syst.*, vol. 53, no. 6, pp. 3070–3078, Dec. 2017.

[28] N. S. Wheadon, J. C. Whitehouse, J. D. Milsom, and R. N. Herring, "Ionospheric modelling and target coordinate registration for HF sky-wave radars," in *Proc. 6th Int. Conf. HF Radio Syst. Techn.*, 1994, pp. 258–266.

[29] T. A. Croft and H. Hoogansian, "Exact ray calculations in a quasi-parabolic ionosphere with no magnetic field," *Radio Sci.*, vol. 3, no. 1, pp. 69–74, 1968, doi: 10.1002/rds19683169.

[30] Z. Lei, J. Chen, H. Chen, Z. Zhang, G. Dou, and Y. Wang, "Reference source-aided coordinate registration method for over-the-horizon radar using ensemble learning," *IET Radar, Sonar, Navigation*, vol. 17, pp. 74–85, 2023, doi: 10.1049/rsn2.12325.

[31] B. W. Reinisch and D. Bilitza, "Karl Rawer's life and the history of IRI," *Adv. Space Res.*, vol. 34, no. 9, pp. 1845–1850, 2004.

[32] T. Thayaparan, J. Marchioni, A. Kelsall, and R. Riddolls, "Improved frequency monitoring system for sky-wave over-the-horizon radar in Canada," *IEEE Geosci. Remote Sens. Lett.*, vol. 17, no. 4, pp. 606–610, Apr. 2020.

[33] L. Perna et al., "Bottom side profiles for two close stations at the southern crest of the EIA: Differences and comparison with IRI-2012 and NeQuick2 for low and high solar activity," *Adv. Space Res.*, vol. 61, no. 1, pp. 295–315, 2018.

[34] H. Chen, L. Liu, W. Wan, B. Ning, and J. Lei, "A comparative study of the bottomside profile parameters over Wuhan with IRI-2001 for 1999–2004," *Earth, Planets, Space*, vol. 58, no. 5, pp. 601–605, 2006.

[35] Y. Chuo, "Variations of ionospheric profile parameters during solar maximum and comparison with IRI-2007 over Chung-Li, Taiwan," *Annales Geophysicae*, vol. 30, pp. 1249–1257, 2012.

[36] D. Altadill, J. M. Torta, and E. Blanch, "Proposal of new models of the bottom-side B0 and B1 parameters for IRI," *Adv. Space Res.*, vol. 43, no. 11, pp. 1825–1834, 2009.

[37] N. K. Sethi, R. S. Dabas, and A. K. Upadhayaya, "Midday bottomside electron density profiles during moderate solar activity and comparison with IRI-2001," *Adv. Space Res.*, vol. 43, no. 6, pp. 973–983, 2009.

[38] K. Venkatesh, P. R. Fagundes, R. de Jesus, A. J. de Abreu, V. G. Pillat, and S. G. Sumod, "Assessment of IRI-2012 profile parameters by comparison with the ones inferred using NeQuick2, ionosonde and FORMOSAT-1 data during the high solar activity over Brazilian equatorial and low latitude sector," *J. Atmospheric Sol.-Terr. Phys.*, vol. 121, pp. 10–23, 2014.

[39] I. S. Batista and M. A. Abdu, "Ionospheric variability at Brazilian low and equatorial latitudes: Comparison between observations and IRI model," *Adv. Space Res.*, vol. 34, no. 9, pp. 1894–1900, 2004.

[40] F. C. P. Bertoni et al., "IRI-2001 model predictions compared with ionospheric data observed at Brazilian low latitude stations," *Annales Geophysicae*, vol. 24, pp. 2191–2200, 2006.

[41] Z. Liu, H. Fang, L. Weng, S. Wang, J. Niu, and X. Meng, "A comparison of ionosonde measured foF2 and IRI-2016 predictions over China," *Adv. Space Res.*, vol. 63, no. 6, pp. 1926–1936, 2019.

[42] C. Shi, T. Zhang, C. Wang, Z. Wang, and L. Fan, "Comparison of IRI-2016 model with IGS VTEC maps during low and high solar activity period," *Results Phys.*, vol. 12, pp. 555–561, 2019.

[43] S. Alcay and G. Oztan, "Analysis of global TEC prediction performance of IRI-PLAS model," *Adv. Space Res.*, vol. 63, no. 10, pp. 3200–3212, 2019.

[44] H. Rishbeth, "How the thermospheric circulation affects the ionospheric F2-layer," *J. Atmospheric Sol.-Terr. Phys.*, vol. 60, no. 14, pp. 1385–1402, 1998.

[45] S. S. Kouris and D. N. Fotiadis, "Ionospheric variability: A comparative statistical study," *Adv. Space Res.*, vol. 29, no. 6, pp. 977–985, 2002.

[46] K. J. Hickey, E. W. Gill, J. A. Helbig, and J. Walsh, "Measurement of ocean surface currents using a long-range, high-frequency ground wave radar," *IEEE J. Ocean. Eng.*, vol. 19, no. 4, pp. 549–554, Oct. 1994.

[47] J. D. Paduan and L. Washburn, "High-frequency radar observations of ocean surface currents," *Annu. Rev. Mar. Sci.*, vol. 5, pp. 115–136, 2013.

[48] Y. Shaolin, K. Hengyu, W. Xiongbin, T. Jiansheng, and H. Jiechang, "HF radar ocean current algorithm based on MUSIC and the validation experiments," *IEEE J. Ocean. Eng.*, vol. 30, no. 3, pp. 601–618, Jul. 2005.

[49] M. Li, X. Wu, L. Zhang, X. Yue, C. Li, and J. Liu, "A new algorithm for surface currents inversion with high-frequency over-the-horizon radar," *IEEE Geosci. Remote Sens. Lett.*, vol. 14, no. 8, pp. 1303–1307, Aug. 2017.

[50] P. L. Dyson and J. A. Bennett, "A model of the vertical distribution of the electron concentration in the ionosphere and its application to oblique propagation studies," *J. Atmospheric Terr. Phys.*, vol. 50, no. 3, pp. 251–262, 1988.

[51] R. J. Norman and P. S. Cannon, "An evaluation of a new two-dimensional analytic ionospheric ray-tracing technique: Segmented method for analytic ray tracing (SMART)," *Radio Sci.*, vol. 34, no. 2, pp. 489–499, 1999, doi: 10.1029/98RS01788.

[52] K. Davies and C. M. Rush, "High-frequency ray paths in ionospheric layers with horizontal gradients," *Radio Sci.*, vol. 20, no. 1, pp. 95–110, 1985, doi: 10.1029/RS020i001p00095.

[53] K. Folkestad, "Exact ray computations in a tilted ionosphere with no magnetic field," *Radio Sci.*, vol. 3, no. 1, pp. 81–84, 2016.

[54] R. M. Jones, "A three-dimensional ray-tracing computer program (Digest of ESSA Technical Report, ITSA No. 17)," *Radio Sci.*, vol. 3, pp. 93–94, 1968.

[55] M. Feng et al., "Research on a simulation model of a skywave over-the-horizon radar sea echo spectrum," *Remote Sens.*, vol. 14, 2022, Art. no. 1461.

[56] Q. Zhou, X. Yue, L. Zhang, X. Wu, and L. Wang, "Correction of ionospheric distortion on HF hybrid sky-surface wave radar calibrated by direct wave," *Radio Sci.*, vol. 54, no. 5, pp. 380–396, 2019.

[57] R. Schmidt, "Multiple emitter location and signal parameter estimation," *IEEE Trans. Antennas Propag.*, vol. TAP-34, no. 3, pp. 276–280, Mar. 1986.

[58] M. Feng, H. Fang, X. Wu, W. Ai, X. Yue, and L. Zhang, "Correction of ionosphere phase contamination of high-frequency hybrid sky-surface wave radar using wavelet transform," *IET Radar, Sonar, Navigation*, vol. 17, pp. 1017–1022, Jun. 2023, doi: 10.1049/rsn2.12396.

Mengyan Feng received the B.S. degree in atmosphere science from Lanzhou University, Lanzhou, China, in 2018, and the M.S. degree in atmosphere science in 2020 from the National University of Defense Technology, Changsha, China, where he is currently working toward the Ph.D. degree in atmosphere science.

His research interests include satellite-borne microwave radiometer remote sensing and high-frequency radar ocean environment remote sensing, which mainly involves the development of atmosphere and ocean environment retrieval algorithms, signal processing technology, and the design of satellite and radar systems.

Hanxian Fang received the M.S. degree in atmosphere science from the PLA University of Science and Technology, Nanjing, China, in 2004.

His research interests include space weather and radar detection research.

Xiongbin Wu received the B.Sc. degree in geophysics from Peking University, Beijing, China, in 1990, and the Ph.D. degree in space physics from Wuhan University, Wuhan, China, in 1999.

Since 1994, he has been involved in high-frequency surface-wave radar (HFSWR) and radio wave propagation studies. He is one of the original contributors to the development of the ocean state monitoring and analyzing radar series HFSWR. He is currently the Principal Investigator of the HFSWR Project in the National High-Tech Research and Development Program of China (863 program), in which an HF hybrid radar network had been built for the purpose of ocean dynamics surveillance in a wider area than the HFSWR covers. He is also a Professor of Radio Physics with the School of Electronic Information, Wuhan University. His research interests include HF/microwave radar remote sensing of ocean dynamics under high sea states and abnormal events, and ionospheric radio wave propagation.

Dr. Wu is a recipient of several awards from the China Ocean Engineering Society, the Ministry of Science and Technology of China, and the Ministry of Education of China.

Weihua Ai received the B.S., M.S., and Ph.D. degrees in atmosphere science from the PLA University of Science and Technology, Nanjing, China, in 2002, 2004, and 2007, respectively.

He is currently an Associate Professor with the College of Atmosphere and Sea, National University of Defense Technology, Changsha, China. His research interests include radar simulators and microwave remote sensing.

Xianchang Yue received the B.S. and M.S. degrees in computational mathematics and the Ph.D. degree in space physics from Wuhan University, Wuhan, China, in 1996, 1999, and 2005, respectively.

Since 2005, he has been an Associate Professor with Electronic Information School, Wuhan University. His research interests include numerical simulation in atmospheric–oceanic dynamics, and ocean wind and wave retrieval from ocean remote sensing by high-frequency radar.

Lan Zhang received the B.Sc. degree in communication engineering, the M.S. degree in signal and information processing, and the Ph.D. degree in radio physics from Wuhan University, Wuhan, China, in 2004, 2006, and 2015, respectively.

She is currently a Senior Experimentalist with the School of Electronic Information, Wuhan University. Her research interests include the design of high-frequency (HF) radar systems and HF radar remote sensing of ocean dynamics parameters.